Article

Ppb-Level Butanone Sensor Based on ZnO-TiO$_2$-rGO Nanocomposites

Zhijia Liao [1], Yao Yu [1,2,3,4], Zhenyu Yuan [1,2,3] and Fanli Meng [1,2,3,*]

1   College of Information Science and Engineering, Northeastern University, Shenyang 110819, China;
    2070705@stu.neu.edu.cn (Z.L.); 1870748@stu.neu.edu.cn (Y.Y.); yuanzhenyu@ise.neu.edu.cn (Z.Y.)
2   Hebei Key Laboratory of Micro-Nano Precision Optical Sensing and Measurement Technology,
    Qinhuangdao 066004, China
3   Key Laboratory of Data Analytics and Optimization for Smart Industry, Northeastern University,
    Ministry of Education, Shenyang 110819, China
4   School of Electronic Information Engineering, Ningxia Institute of Science and Technology,
    Shizuishan 753000, China
*   Correspondence: mengfanli@ise.neu.edu.cn

Abstract: In this paper, ZnO-TiO$_2$-rGO nanocomposites were successfully synthesized by the hydrothermal method. The morphology and structure of the synthesized nanomaterials were characterized by SEM, XRD, HRTEM, and XPS. Butanone is a typical ketone product. The vapors are extremely harmful once exposed, triggering skin irritation in mild cases and affecting our breathing in severe cases. In this paper, the gas-sensing properties of TiO$_2$, ZnO, ZnO-TiO$_2$, and ZnO-TiO$_2$-rGO nanomaterials to butanone vapor were studied. The optimum operating temperature of the ZnO-TiO$_2$-rGO sensor is 145 °C, which is substantially lower than the other three sensors. The selectivity for butanone vapor is greatly improved, and the response is 5.6 times higher than that of other organic gases. The lower detection limit to butanone can reach 63 ppb. Therefore, the ZnO-TiO$_2$-rGO sensor demonstrates excellent gas-sensing performance to butanone. Meanwhile, the gas-sensing mechanism of the ZnO-TiO$_2$-rGO sensor to butanone vapor was also analyzed.

Keywords: zinc oxide; graphene; butanone; titanium dioxide

1. Introduction

Butanone is a colorless and transparent liquid with a slight odor and volatility [1], which is widely used in industrial production [2]. The exposure of butanone vapor to open flame or high temperature can cause combustion and explosion, resulting in accidental injury or death [3]. Without direct contact with butanone vapor, it will also bring certain stimulation and harm to our body. It is even genotoxic and carcinogenic, which seriously endangers human health [4,5]. Therefore, it is very important for butanone sensor to achieve early warning detection. In recent years, there has been an increasing interest in VOC sensors with selectivity, high sensitivity, and low cost [6]. However, fewer studies have been reported on the use of gas sensors for butanone measurement [7–10]. These sensors operate at high temperatures, have poor selectivity, and cannot detect lower concentrations. Therefore, it is necessary to develop better sensors to detect the performance of butanone.

Zinc oxide (ZnO) is an n-type semiconductor oxide with a wide band gap (3.37 eV) [11]. It can detect gases under different environmental conditions and has high sensitivity. So, it is widely used in semiconductor oxide-type gas sensors. ZnO nanomaterials have various morphologies, such as rods, spheres, and flowers [12–14]. However, studies have shown that the prepared ZnO-sensing materials still have disadvantages such as high operating temperature and poor target gas selectivity [15–17], which hinder their practical application in the field of gas sensors. So, we searched for other metal oxides for compounding [18–20]. Semiconductor materials such as titanium dioxide (TiO$_2$) have a wide band gap of about 3.0 eV. It is widely used in energy utilization and catalytic research because of its high catalytic activity, non-toxic, good chemical stability, and low price [21–24]. With the

increasing level of scientific research, the properties of pure ZnO and TiO_2 can no longer meet the required requirements. After continuous exploration, the related properties can be improved through the doping mechanism [25]. Park et al. prepared TiO_2-ZnO core–shell nanofibers as sensing materials for the dynamic detection of oxygen [26]. It is found that it has good sensitivity and reproducibility.

Graphene is a two-dimensional honeycomb carbon material composed of single-layer carbon atoms. It has good conductivity [27], rich sources [28], and high thermal conductivity [29]. Graphene has large specific surface area [30] and good adsorption activity [31] due to its single-layer folded structure [32]. As a result of its unique properties, it has a wide range of applications in the field of electronic sensing. Metal oxides generally face problems such as high working temperature and poor selectivity to organic gases. To avoid defects, we intended to introduce the two-dimensional material graphene, forming the ternary nanomaterial ZnO-TiO_2-rGO. Johra et al. in 2015 have prepared RGO-TiO_2-ZnO nanocomposites by the hydrothermal reduction method as a photocatalytic application [33].

In this paper, a simple hydrothermal method was used to prepare the ternary nano-material ZnO-TiO_2-rGO for gas sensor applications. The ZnO-TiO_2-rGO sensor has good stability, reproducibility, and selectivity for butanone vapor at low temperatures. The sensor is also capable of detecting lower butanone vapors and has good selectivity to butanone vapors. The ternary composite nanomaterial ZnO-TiO_2-rGO significantly improved its gas-sensitive performance.

2. Materials and Characterization Instruments

2.1. Reagents and Instruments

$C_{12}H_{28}O_4Ti$ (AR) and CH_3COOH (AR) were both purchased from Shanghai Macklin Biochemical Co., Ltd. NaOH (AR) and $(CH_3COO)_2Zn$ (AR) were both purchased from Sinopharm Group Chemical Reagent Co., Ltd. C_2H_5OH (AR) was purchased from Tianjin Fuyu Fine Chemical Co., Ltd. AR is analytical pure reagent. The microscopic morphology and crystal structure of the nanomaterials were characterized and imaged using the instruments such as high-resolution transmission electron microscopy (HRTEM, JEOLJEM-2010, Beijing, China), X-ray photoelectron spectrometry (XPS, Thermo Scientific[TM] K-Alpha[TM+] spectrometer, Beijing, China), field-emission scanning electron microscopy (SEM, Hitachi, Tokyo, Japan), and X-ray diffraction (XRD, SmartLab SE, Tokyo, Japan).

2.2. Materials Preparation

First, 1.5 mL of $C_{12}H_{28}O_4Ti$, 50 mL of C_2H_5OH, and 1 mL of CH_3COOH were mixed in the same beaker and sonicated for 20 min. The mixed solution was loaded into the reactor and reacted at 200 °C for 1 h. The product obtained was dried at 60 °C by centrifuging twice with water and ethanol, respectively. This process yielded the nanomaterial TiO_2.

Then, 270 mg $(CH_3COO)_2Zn$ was stirred well with 50 mL of deionized water, and 1 M NaOH solution was added dropwise to pH = 12. The mixed solution was poured into a suitable capacity reactor and reacted at 200 °C for 1 h. The same was centrifuged and dried at 60 °C. This process yields the product ZnO.

Then, 1.5 mL of $C_{12}H_{28}O_4Ti$, 50 mL of C_2H_5OH, and 1 mL of CH_3COOH were mixed in the same beaker and sonicated for 20 min. The mixed solution was loaded into the reaction kettle and reacted at 200 °C for 1 h. After centrifuging twice with water and ethanol respectively, 100 mL of deionized water was added and stirred well. Then, we added 270 mg of $(CH_3COO)_2Zn$ and 1 M NaOH solution drop by drop to pH = 12. Afterwards, we poured the mixed solution into a suitable capacity reaction kettle, let it react for 1 h at 200 °C, performed centrifugation, and let it dry at 60 °C. This experimental procedure yielded the product ZnO-TiO_2.

Graphene oxide was prepared by a modified Hummers method. First, 4 g of graphite raw material was placed in a 500 mL beaker. Then, 70 mL of concentrated sulfuric acid was added to the beaker, and the mouth of the beaker was sealed with plastic wrap. The beaker was placed on a magnetic mixer and stirred vigorously for 1 h to fully react the graphite

with the concentrated sulfuric acid. Then, 12 g of KMnO$_4$ was slowly added to the mixed solution. The beaker was placed in a warm water bath at 35 °C for 6 h. Afterwards, 100 mL of deionized water was added to the beaker and stirred for 30 min. Then, 40 mL of 30% hydrogen peroxide was added, and the solution turned golden yellow. Then, 30 mL of 1 mol/L HCl and 200 mL of deionized water were added and stirred for 30 min. Finally, the solution was washed by centrifugation with deionized water to neutral [34,35]. In addition, 6.5 mg/mL of graphene oxide was prepared for use. First, 1.5 mL of C$_{12}$H$_{28}$O$_4$Ti, 50 mL of C$_2$H$_5$OH, and 1 mL of CH$_3$COOH were mixed in a beaker and sonicated for 20 min. Then, 1.5 mL of 6.5 mg/mL GO was added and stirred evenly. The solution was put into the reactor and reacted at 200 °C for 1 h. After centrifuging twice with water and ethanol, 100 mL of deionized water and 270 mg of (CH$_3$COO)$_2$Zn were added. Then, 1 M NaOH was added dropwise to the solution until pH = 12. The mixed solution was put into the reactor and reacted at 200 °C for 1 h. Finally, the sample was dried at 60 °C and collected. The ideal ternary nanomaterial ZnO-TiO$_2$-rGO was obtained [36]. The experimental procedure is illustrated in Figure 1.
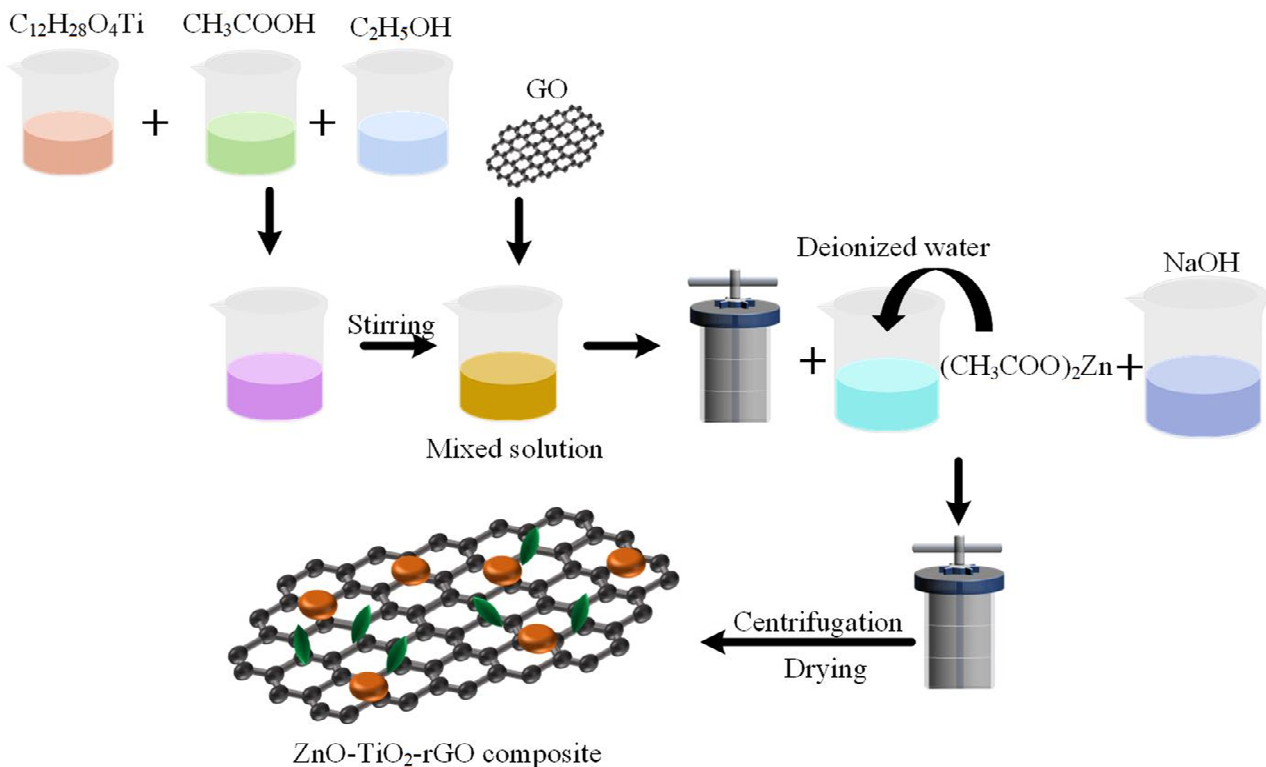

Figure 1. Schematic diagram of the synthesis of ZnO-TiO$_2$-rGO nanomaterials.

2.3. Fabrication and Testing of Sensors

For gas testing, the entire system consists of a synthetic dry air unit, a programmable DC power supply (RIGOL DP832A), a digital source meter (Keysight B2902A), and a 1 L gas chamber. The synthetic dry air consists of 21% oxygen and 79% nitrogen. The programmable DC power supply controls and regulates the temperature to which the sensor is adapted by connecting a resistive wire through an electrode. A digital source meter displays the current and voltage of the sensor during operation, and the change in resistance of the sensor during operation is displayed and recorded by the Labview software in the computer. The sensor is affected by the entry and exit of air and target gas in the confined chamber, and its resistance magnitude varies with some regularity. The

target gas is the vapor pressure of different substances at different temperatures calculated using Antoine's formula, as shown in Equation (1).

$$\log_{10} P = A - B/(T + C) \tag{1}$$

where P is the vapor pressure of the substance in mmHg. T is the temperature in $^\circ$C. B and C are the corresponding constant coefficients. By calculation, the saturation vapor pressure of some organic gases will have a corresponding volume, and experiments will be performed with different sizes of syringes.

The sensor is shown in Figure 2 and consists of a ceramic tube, Ni-Cr heater, a gold electrode, and a platinum wire. The prepared nanomaterials were mixed well with a small amount of ethanol and applied to the surface of the ceramic tube to measure the gas-sensitive properties of the gas. The response of the gas sensor to the target gas is defined by Equation (2):

$$S = \frac{R_g - R_a}{R_a} \times 100\% \tag{2}$$

where S is the sensitivity of the gas sensor and also the response value of the gas sensor. R_g is the resistance value displayed by the gas sensor in the test gas. R_a is the resistance value displayed by the gas sensor in air.
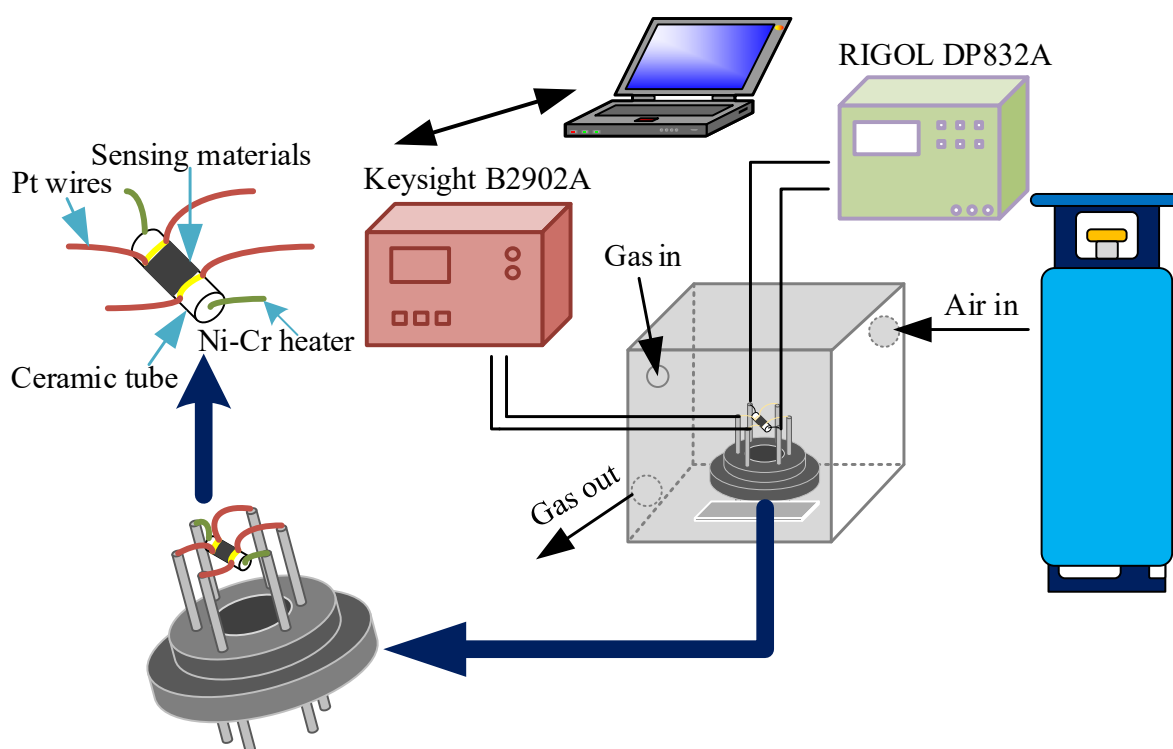

Figure 2. Schematic diagram of the gas sensor.

3. Results and Discussion

3.1. Characterization

The SEM image of Figure 3a shows that ZnO-TiO$_2$ is composed of ZnO nanorods and TiO$_2$ nanoparticles. ZnO nanorods are dispersed in the surrounding environment. TiO$_2$ nanoparticles are small in size and randomly stacked together. Figure 3b shows the SEM image of graphene oxide. It can be seen that graphene oxide is layered, similar to a thin film. It has very obvious folds. The SEM image in Figure 3c is ZnO-TiO$_2$-rGO ternary nano material. ZnO nanorods and TiO$_2$ nanoparticles are wrapped by graphene film. In addition, it can be seen that the size of TiO$_2$ nanoparticles gradually increases and becomes obviously spherical. It indicated that in the composite process of ZnO-TiO$_2$-rGO ternary

nanomaterials, the formation of ZnO nanorods and TiO_2 nanoparticles gradually changes due to the existence of graphene. Figure 3d shows the elemental contents corresponding to the EDS plots. It demonstrates that the ternary nanomaterial $ZnO-TiO_2$-rGO adequately contains elements C, O, Ti, and Zn without the interference of other clutter elements. The percentages of elemental C, O, Ti, and Zn contents are listed in Table 1.
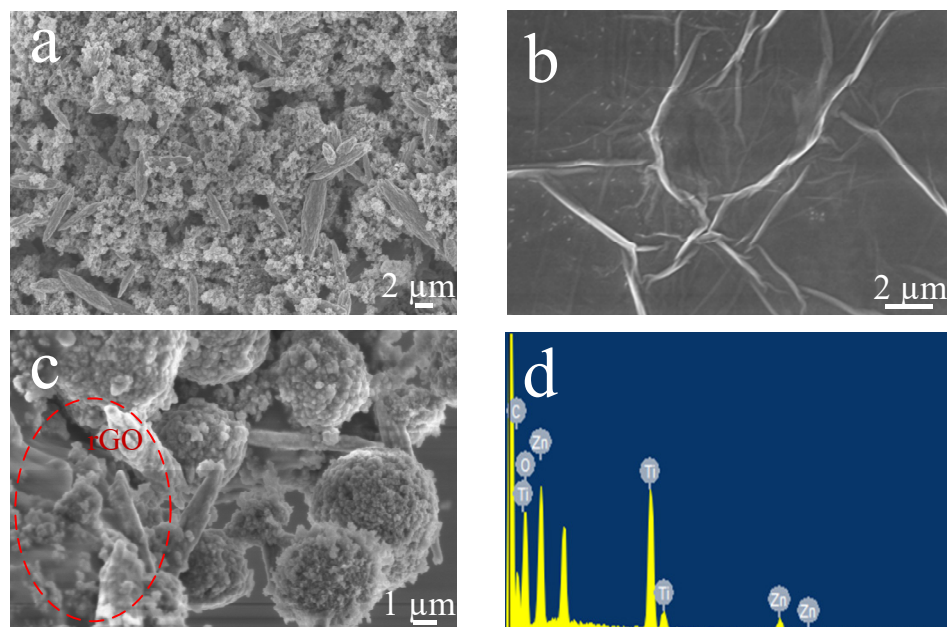

Figure 3. SEM images of (**a**) $ZnO-TiO_2$, (**b**) GO, and (**c**) $ZnO-TiO_2$-rGO. (**d**) Element content of $ZnO-TiO_2$-rGO.

Table 1. Element content of $ZnO-TiO_2$-rGO.

Element	Weight %	Atom %
C	20.97	36.47
O	36.19	47.26
Ti	22.17	9.67
Zn	20.67	6.60
Totals	100.00	100.00

Figure 4 shows the elemental mapping part of $ZnO-TiO_2$-rGO. Figure 4a mainly shows the elemental mapping of the ZnO rod range. Figure 4b mainly shows the elemental mapping of the TiO_2 sphere range. It is more accurate to see that the previous SEM of $ZnO-TiO_2$-rGO has ZnO in the rod range and TiO_2 in the sphere range. For ZnO, the rod elements are basically Zn and O. For TiO_2 spherical particles, the O, Ti, and Zn contents are more, indicating that for the most spherical TiO_2, ZnO rods are more exposed. It can be clearly seen that the background element is C for both ZnO rods and TiO_2 spheres, indicating that ZnO rods and TiO_2 spheres are grown on the graphene oxide film. It is also proved that the elemental composition of $ZnO-TiO_2$-rGO ternary nanomaterials is Zn, Ti, O, and C.

Figure 5a shows the XRD patterns of four nanomaterials, ZnO, TiO_2, $ZnO-TiO_2$, and $ZnO-TiO_2$-rGO. ZnO displays characteristic diffraction peaks at $2\theta = 31.25°, 34.72°, 36.36°, 47.83°, 54.55°$, and $62.83°$. They correspond to the crystal planes (100), (002), (101), (102), (110), and (103) of PDF#99-0111, respectively. TiO_2 exhibits characteristic diffraction peaks at $2\theta = 25.36°, 37.98°, 48.16°, 55.25°$, and $62.96°$, corresponding to the crystallographic planes (101), (004), (200), (211), and (204) of PDF#99-0008, respectively. The $ZnO-TiO_2$ binary nanocomposites show diffraction peaks at $25.36°, 31.94°, 34.49°, 36.44°, 47.85°, 56.89°$, and $63.05°$ [37]. The presence of ZnO with TiO_2 is demonstrated. Figure 5b shows

the ZnO-TiO$_2$-rGO HRTEM image. After the experimental calculation by the software Gatan DigitalMicrograph, the lattice spacing of ZnO is 0.26 nm, which corresponds to the crystal plane of ZnO in XRD (100). The lattice spacing of TiO$_2$ is 0.30 nm, which corresponds to the crystal plane of TiO$_2$ in XRD (101) [38].
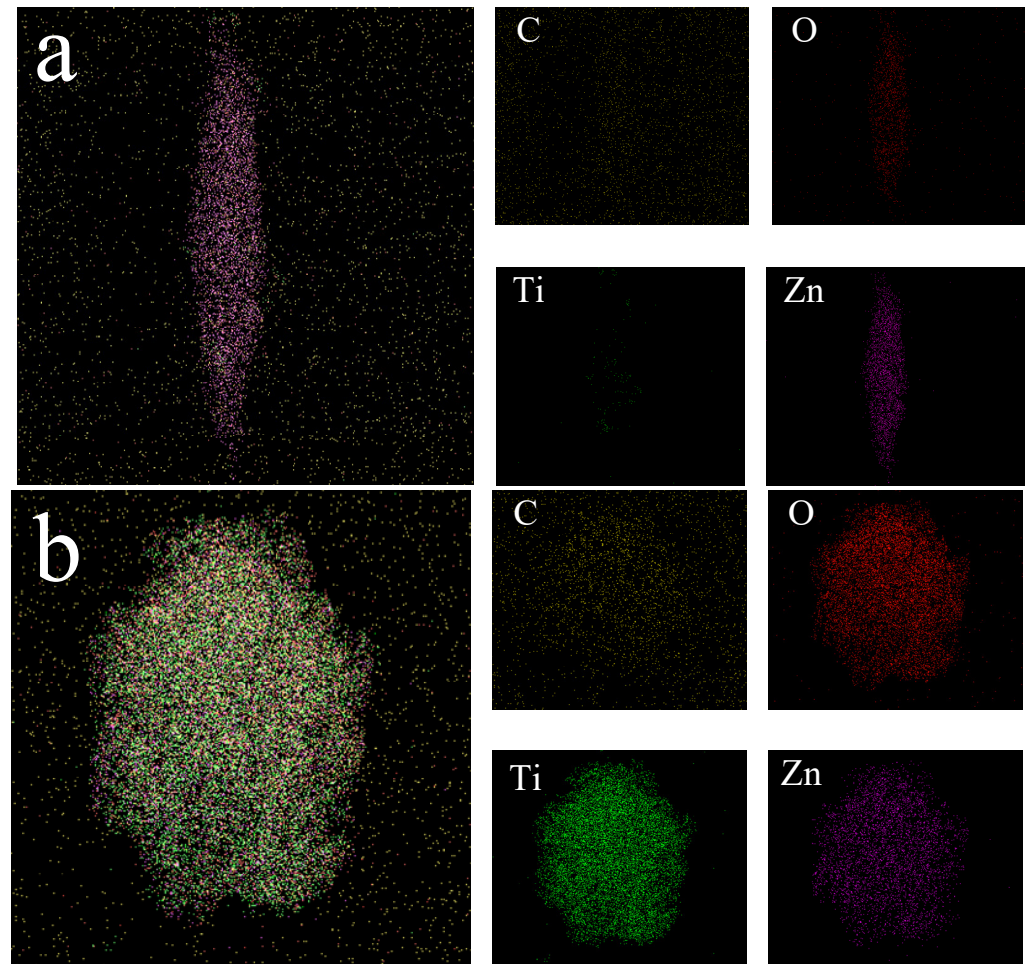

Figure 4. (**a**) ZnO-TiO$_2$-rGO elemental mapping of rod-shaped ZnO. (**b**) ZnO-TiO$_2$-rGO elemental mapping of spherical TiO$_2$.
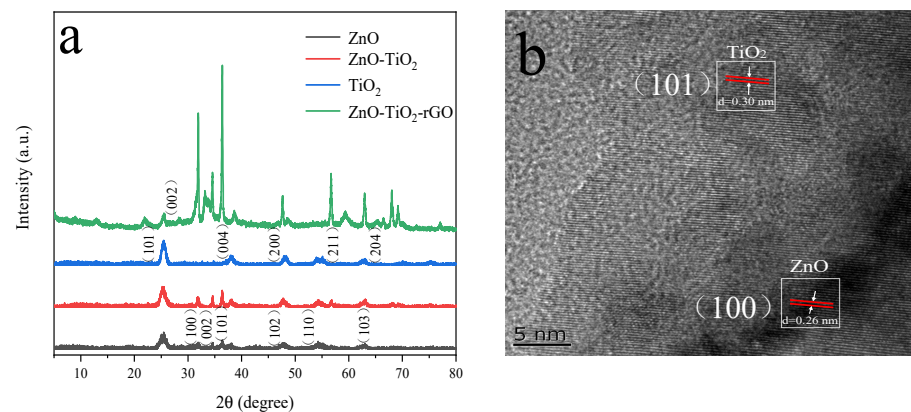

Figure 5. (**a**) XRD patterns of ZnO, TiO$_2$, ZnO-TiO$_2$, and ZnO-TiO$_2$-rGO. (**b**) TEM high-resolution image of ZnO-TiO$_2$-rGO.

XPS can provide in-depth analysis of the surface composition and elemental composition of solid samples. Figure 6 shows the XPS spectrum of ZnO-TiO$_2$-rGO. Figure 6a

shows the full spectrum of ZnO-TiO$_2$-rGO. It can be seen that Zn 2p, Ti 2p, C 1s, and O 1s show peaks at the binding of 1020.5 eV, 459.4 eV, 284.7 eV, and 530.3 eV, respectively [39]. Figure 6b shows the Zn 2p mapping of the nanocomposites. The binding energies of 1020.9 eV and 1043.8 eV correspond to Zn 2p$_{3/2}$ and Zn 2p$_{1/2}$, respectively. Figure 6c provides the Ti 2p mapping of the nanocomposite, showing two peaks centered at 457.6 eV and 463.4 eV for Ti 2p$_{3/2}$ and Ti 2p$_{1/2}$, respectively [40]. Figure 6d shows the C 1S diagram of the nanocomposite. The peak at the sp2 carbon atom belongs to graphene oxide, and the peak at 284.5 eV corresponds to C = C. The peak at the higher binding energy corresponds to C = O (287.8 eV) [41]. This result reinforces the successful composite of ZnO-TiO$_2$-rGO nanocomposites.
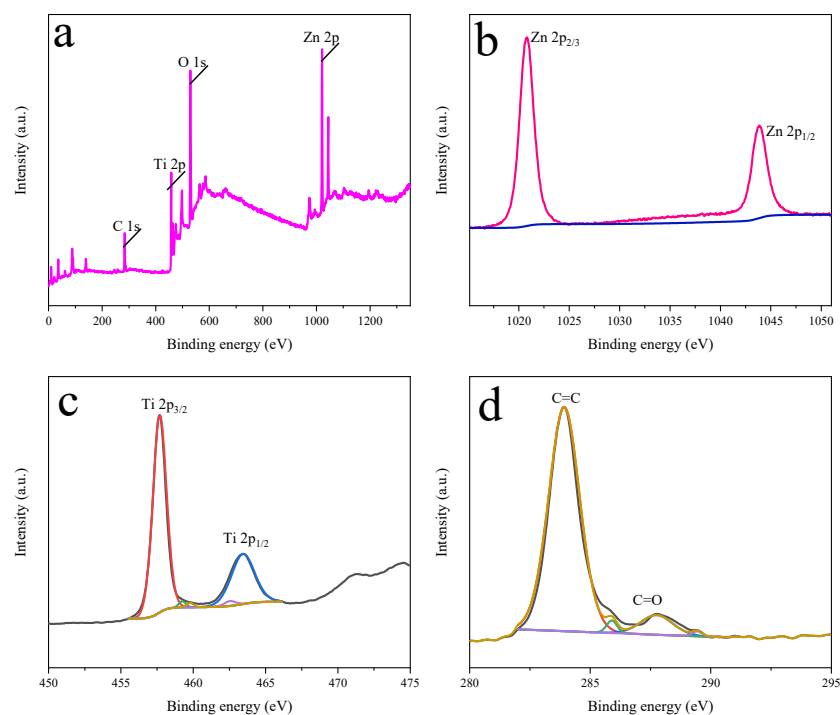

Figure 6. (**a**) Measured spectrum of ZnO-TiO$_2$-rGO. (**b**) XPS spectrum of Zn. (**c**) XPS spectrum of Ti. (**d**) XPS spectrum of C.

Figure 7 shows the infrared spectra of ZnO-TiO$_2$-rGO before and after comparison with the passage of butanone vapor. The wavelength is around 667 cm^{-1} for the Ti-O-Ti bond vibration absorption peak [42]. The C = C bond at a number of 1623 cm^{-1} and the C-O bond at a wavelength of 1048 cm^{-1} can be seen in the figure [43]. By comparing the two figures, it can be observed that the intensity of the peaks in the other ranges gradually decreases, but the peak at 1048 cm^{-1} is enhanced for the C-O bond, where O is the element in butanone and C is the element in GO. It is equivalent to the C = O bond breaking and changing to a C-O bond in this process. It indicates that the ZnO-TiO$_2$-rGO ternary nanomaterial sensor is in contact with the GO phase when it is in contact with the butanone vapor.

Figure 7 shows the infrared spectra of ZnO-TiO$_2$-rGO before and after comparison with the passage of butanone vapor. The wavelength is around 667 cm^{-1} for the Ti-O-Ti bond vibration absorption peak [42]. The C = C bond at 1623 cm^{-1} and the C-O bond at a wavelength of 1048 cm^{-1} can be seen in the figure [43]. By comparing the two figures, it can be observed that the intensity of the peaks in the other ranges gradually decreases, but the peak at 1048 cm^{-1} is enhanced for the C-O bond, where O is the element in butanone and C is the element in GO. It is equivalent to the C = O bond breaking and changing to a C-O bond in this process. It indicates that the ZnO-TiO$_2$-rGO ternary nanomaterial sensor is in contact with the GO phase when it is in contact with the butanone vapor.
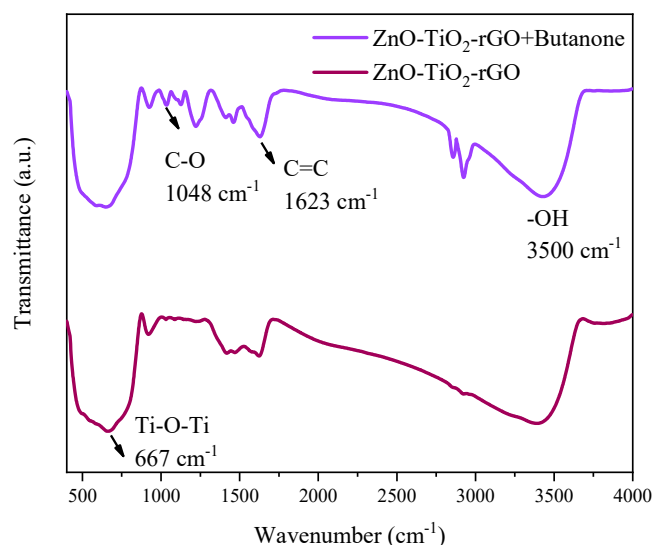
Figure 7. Infrared spectra of ZnO-TiO$_2$-rGO before and after the passage of butanone vapor.

3.2. Gas-Sensing Properties

The sensitivity of the sensors is influenced by the operating temperature, because the change of temperature affects the response of the nanomaterials. We measured different sensors in roughly the same range of temperatures. The optimal operating temperatures of the different sensors are also shown in Figure 8a. The optimum operating temperatures of the ZnO sensor, TiO$_2$ sensor, ZnO-TiO$_2$ sensor, and ZnO-TiO$_2$-rGO sensor are 336 °C, 323 °C, 390 °C, and 145 °C, respectively. It can be clearly seen that the optimal operating temperature of the ZnO-TiO$_2$-rGO sensor is greatly reduced compared to the optimal operating temperature of the other three sensors. The lower energy consumption is more conducive to the development of practical applications. Gas sensors will respond to different organic gases to different degrees. The sensitivity of ZnO, TiO$_2$, ZnO-TiO$_2$, and ZnO-TiO$_2$-rGO to eight different organic gases is shown in Figure 8b. Although the ZnO sensor has a high response to butanone vapor, it still has a high response to other organic gases, such as alcohols and ketones. This also indicates that the selectivity of the ZnO sensor is poor. The response of the TiO$_2$ sensor to xylene and butanone is very high, and even the response to xylene has exceeded that of butanone. The response of the ZnO-TiO$_2$ sensor to butanone is 1.93 times that of other organic gases. However, the response of the ZnO-TiO$_2$-rGO sensor to butanone is the highest, which is 5.6 times that of other organic gases. Figure 8c shows the concentration gradient graph of the ZnO-TiO$_2$-rGO sensor. There are corresponding 9.72%, 13%, 18.2%, 22.06%, and 38.69% values for butanone vapor concentrations of 10 ppm, 25 ppm, 50 ppm, 75 ppm, and 150 ppm, respectively. Figure 8d shows the recovery curve of the response of the ZnO-TiO$_2$-rGO sensor to the lowest concentration of butanone vapor. A butanone vapor of 63 ppb can be detected with a response of 1.3%. Figure 8e shows more clearly the variation of the response values of the ZnO-TiO$_2$-rGO sensor for different butanone vapor concentrations as well as the fitted curves for the responses of different butanone concentrations. The fitted curve is $y = 6.43 + 0.21x$, where x is the different concentrations of butanone vapor and y is the corresponding fitted response value. Figure 8f shows the test of the ZnO-TiO$_2$-rGO sensor under different humidity environments. A certain humidity atmosphere is achieved by proportioning saturated salt solution. The response values of the ZnO-TiO$_2$-rGO sensor corresponding to 27.5%, 25.3%, 24.3%, and 16.4% at 6.6%, 26%, 56%, and 95% humidity are demonstrated. It can be seen that the response value of the ZnO-TiO$_2$-rGO sensor decreases slightly with the increase in humidity. Considered together, the ZnO-TiO$_2$-rGO sensor exhibits good gas-sensitive performance for butanone vapor in terms of operating temperature, directional selectivity, and minimum detection line. Table 2 shows that the SiO$_2$@CoO core–shell sensor has a high response to butanone, but the working temperature

of the sensor is very high, which is 350 °C. The 2% Pt/ZnO sensor also has a high response to butanone, but the working temperature of the sensor is very high, and the detection line is 5 ppm. Overall, the ZnO-TiO$_2$-rGO sensor has a higher butanone-sensing performance.
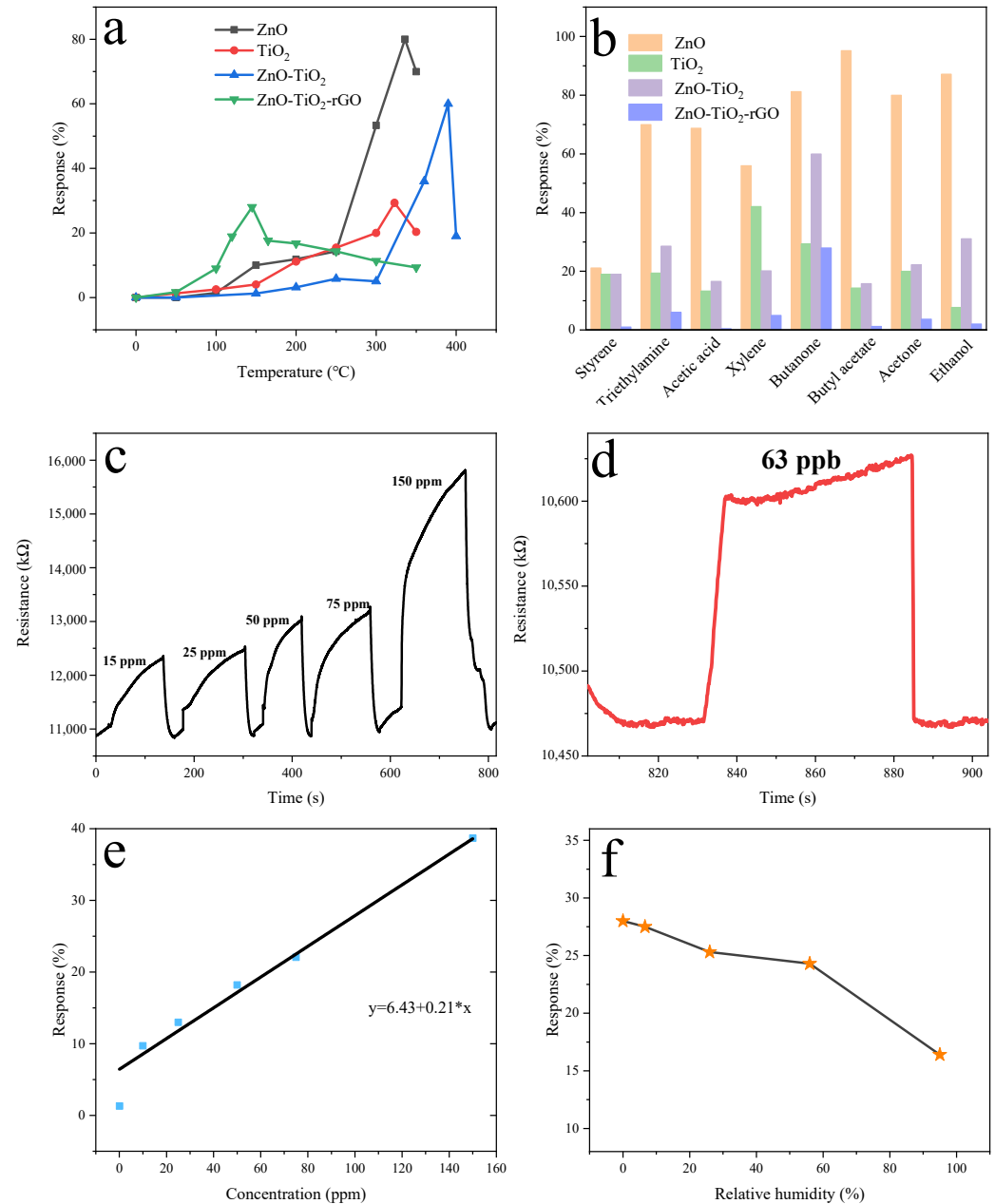

Figure 8. (**a**) Optimal operating temperatures for ZnO, TiO$_2$, ZnO-TiO$_2$, and ZnO-TiO$_2$-rGO sensors. (**b**) Response of ZnO, TiO$_2$, ZnO-TiO$_2$, and ZnO-TiO$_2$-rGO sensors to different gases at 100 ppm. (**c**) ZnO-TiO$_2$-rGO sensor response versus butanone concentration. (**d**) Minimum lower limit of ZnO-TiO$_2$-rGO sensor. (**e**) The sensitivity-fitting curves of ZnO-TiO$_2$-rGO for different concentrations of butanone. (**f**) Humidity curve of the ZnO-TiO$_2$-rGO sensor.

3.3. Gas-Sensing Mechanism of the ZnO-TiO$_2$-rGO

For ZnO-TiO$_2$ binary metal oxides, filling with graphene oxide and its composite greatly improves the gas-sensitive performance of the sensor to butanone. Here, rGO enhances the adsorption for ZnO nanorods and TiO$_2$ nanoparticles grow firmly on the film of rGO. Moreover, TiO$_2$ transforms from nanoparticles to spheres, increasing the overall specific surface area. For the butanone vapor, it can contact with the rGO film and increase

the contact sites. Meanwhile, rGO enhances the electrical conductivity and the transfer of electrons during gas transport. The results show that the presence of graphene reduces the detection limit of butanone vapor.

Table 2. Comparison of the sensing performance toward the detection of butanone of different sensors.

Materials	Butanone Concentration (ppm)	Response	Operating Temperature (°C)	Low Detection Limit	Reference
TiO_2 nanoflowers	700	$1.18(R_a/R_g)$	60	Not mentioned	6
2% Pt/ZnO twin-rods	100	$35.2(R_a/R_g)$	450	5 ppm	7
ZnO bicone	100	$29.4(R_a/R_g)$	400	0.41 ppm	8
WO_3-Cr_2O_3 nanorods	100	$5.6(R_a/R_g)$	205	5 ppm	9
SiO_2@CoO core shell	100	$44.7(R_a/R_g)$	350	Not mentioned	10
ZnO-TiO_2-rGO	100	$28.9\%(\Delta R/R_a)$	145	63 ppb	This work

4. Conclusions

In this paper, ZnO-TiO_2-rGO ternary composites were prepared by the hydrothermal method. For experimental comparison, ZnO, TiO_2, and ZnO-TiO_2 nanomaterials were also prepared for gas-sensitive testing. The morphology and structure of the four synthesized nanomaterials were also characterized by XPS, HRTEM, SEM, and XRD. The results show that the ternary ZnO-TiO_2-rGO nanomaterials have an optimal sensor operating temperature of 145 °C and a response of 28% to 100 ppm butanone vapor. Not only can butanone vapor be detected at 63 ppb but also the ternary ZnO-TiO_2-rGO nanomaterials have better selectivity than ZnO, TiO_2, and ZnO-TiO_2 nanomaterials. Therefore, the experimental results show that the ZnO-TiO_2-rGO sensor has better sensing performance to butanone vapor.

References

1. Zhang, Q.; Xu, M.; Shen, Z.; Wei, Q. A nanostructured Cr_2O_3/WO_3 p–n junction sensor for highly sensitive detection of butanone. *J. Mater. Sci. Mater. Electron.* **2017**, *128*, 12056–12062. [CrossRef]
2. Liu, X.; Qin, X.; Ji, H.; Wang, M. An enhanced butanone sensing performance of $Er_{0.7}Yb_{0.3}FeO_3$ material with the proper electronic structure. *J. Alloys Compd.* **2018**, *772*, 263–271. [CrossRef]
3. Jiang, Z.; Guo, Z.; Sun, B.; Jia, Y.; Li, M.; Liu, J. Highly sensitive and selective butanone sensors based on cerium-doped SnO_2 thin films. *Sens. Actuators B Chem.* **2010**, *145*, 667–673. [CrossRef]
4. Xu, D.; Ge, K.; Qi, S.; Chen, Y.; Liu, Q. Hydrangea-like mesoporous WO_3 nanoflowers with crystalline framework for 3-hydroxy-2-butanone sensing. *Anal. Bioanal. Chem.* **2020**, *412*, 1–8. [CrossRef] [PubMed]
5. György, S.; Mihály, B. Catalytic transfer hydrogenation of 2-butanone over oxide catalysts. *React. Kinet. Mech. Cat.* **1999**, *68*, 197–205.
6. Bhowmik, B.; Manjuladevi, V.; Gupta, R.; Bhattacharyya, P. Highly Selective Low-Temperature Acetone Sensor Based on Hierarchical 3-D TiO_2 Nanoflowers. *IEEE Sens. J.* **2016**, *16*, 3488–3495. [CrossRef]

7.   Oliveira, T.; Zito, C.; Perfecto, T.; Azevedo, G.; Volanti, D. ZnO twin-rods decorated with Pt nanoparticles for butanone detection. *New J. Chem.* **2020**, *44*, 15574–15583. [CrossRef]

8.   Zito, C.; Perfecto, T.; Oliveira, T.; Volanti, D. Bicone-like ZnO structure as high-performance butanone sensor. *Mater. Lett.* **2018**, *223*, 142–145. [CrossRef]

9.   Zhang, Q.; Zhang, H.; Xu, M.; Shen, Z.; Wei, Q. A WO_3 nanorod-Cr_2O_3 nanoparticle composite for selective gas sensing of 2-butanone. *Chin. Chem. Lett.* **2018**, *29*, 538–542. [CrossRef]

10.   Vioto, G.; Perfecto, T.; Zito, C.; Volanti, D. Enhancement of 2-butanone sensing properties of SiO_2@CoO core-shell structures. *Ceram. Int.* **2020**, *46*, 22692–22698. [CrossRef]

11.   Shih, B.; Xue, Y.; Zhang, P.; Cohen, M.; Louie, S. Quasiparticle band gap of ZnO: High accuracy from the conventional GW approach. *Phys. Rev. Lett.* **2010**, *105*, 146401. [CrossRef]

12.   Qin, W.; Yuan, Z.; Gao, H.; Zhang, R.; Meng, F. Perovskite-structured $LaCoO_3$ modified ZnO gas sensor and investigation on its gas sensing mechanism by first principle. *Sens. Actuators B Chem.* **2021**, *341*, 130015. [CrossRef]

13.   Vayssieres, L. Growth of Arrayed Nanorods and Nanowires of ZnO from Aqueous Solutions. *Adv. Mater.* **2010**, *15*, 464–466. [CrossRef]

14.   Heinlaan, M.; Ivask, A.; Blinova, I.; Dubourguier, H.; Kahru, A. Toxicity of nanosized and bulk ZnO, CuO and TiO_2 to bacteria Vibrio fischeri and crustaceans Daphnia magna and Thamnocephalus platyurus. *Chemosphere* **2008**, *71*, 1308–1316. [CrossRef] [PubMed]

15.   Zhang, S.; Wei, S.; Zunger, A. Intrinsic N-Type Versus P-Type Doping Asymmetry and the Defect Physics of ZnO. *Phys. Rev. B* **2001**, *63*, 075205. [CrossRef]

16.   Wang, Z.; Qian, X.; Yin, J.; Zhu, Z. Large-scale fabrication of tower-like, flower-like, and tube-like ZnO arrays by a simple chemical solution route. *Langmuir* **2004**, *20*, 3441–3448. [CrossRef]

17.   Wang, X.; Zhou, J.; Song, J.; Jin, L.; Zhong, L. Piezoelectric Field Effect Transistor and Nanoforce Sensor Based on a Single ZnO Nanowire. *Nano Lett.* **2006**, *6*, 2768–2772. [CrossRef]

18.   Meng, F.; Qi, T.; Zhang, J.; Zhu, H.; Yuan, Z.; Liu, C.; Qin, W.; Ding, M. MoS_2-templated porous hollow MoO_3 microspheres for highly selective ammonia sensing via a Lewis acid-base interaction. *IEEE Trans. Ind. Electron.* **2021**. Available online: https://ieeexplore.ieee.org/abstract/document/9339981/ (accessed on 2 October 2021). [CrossRef]

19.   Yuan, Y.; Adimi, S.; Thomas, T.; Wang, J.; Guo, H.; Chen, J.; Attfield, J.; DiSalvo, F.; Yang, M. Co_3Mo_3N—An efficient multifunctional electrocatalyst. *Innovation* **2021**, *2*, 40–46.

20.   Ji, H.; Qin, W.; Yuan, Z.; Meng, F. Qualitative and quantitative recognition method of drug-producing chemicals based on SnO_2 gas Sensor with dynamic measurement and PCA weak separation. *Sens. Actuators B Chem.* **2021**, *348*, 130698. [CrossRef]

21.   Shao, X.; Wang, H.; Yuan, M.; Yang, J.; Zhan, W.; Wang, L.; Guo, Y.; Lu, G. Thermal stability of Si-doped V_2O_5/WO_3–TiO_2 for selective catalytic reduction of NO_x by NH_3. *Rare Metals* **2019**, *38*, 292–298. [CrossRef]

22.   Abbas, M.; Zubair, A.; Riaz, K.; Huang, W.; Zubair, M. Engineering multimodal dielectric resonance of TiO_2 based nanostructures for high-performance refractive index sensing applications. *Biomed. Opt. Express* **2020**, *28*, 23509–23522. [CrossRef]

23.   Wang, F.; Shen, B.; Zhu, S.; Wang, Z. Promotion of Fe and Co doped Mn-Ce/TiO_2 catalysts for low temperature NH_3-SCR with SO_2 tolerance. *Fuel* **2019**, *249*, 54–60. [CrossRef]

24.   Taghvaei, N.; Taghvaei, E.; Askari, M. Synthesis of Anodized TiO_2 Nanotube Arrays as Ion Sieve for Lithium Extraction. *ChemistrySelect* **2020**, *5*, 10339–10345. [CrossRef]

25.   Wang, N.; Sun, C.; Zhao, Y.; Zhou, S.; Chen, P.; Jiang, L. Fabrication of three-dimensional ZnO/TiO_2 heteroarchitectures via a solution process. *J. Mater. Chem. A* **2008**, *18*, 3909–3911. [CrossRef]

26.   Park, J.; Sun, W.; Lee, J.; Kim, S. Synthesis and Gas Sensing Properties of TiO_2–ZnO Core-Shell Nanofibers. *J. Am. Ceram. Soc.* **2010**, *92*, 2551–2554. [CrossRef]

27.   Yuan, Z.; Liu, Y.; Zhang, J.; Zhang, H. Rose-like MoO_3/MoS_2/rGO low temperature ammonia sensors based on multi-gas detection methods. *IEEE Trans. Instrum. Meas.* **2021**, *70*, 1–9.

28.   Meng, F.; Li, X.; Yuan, Z.; Lei, Y.; Qi, T.; Li, J. Ppb-Level Xylene Gas Sensors based on Co_3O_4 Nanoparticles coated Reduced Graphene Oxide(rGO) Nanosheets Operating at Low Temperature. *IEEE Trans. Instrum. Meas.* **2021**, *70*, 1–10.

29.   Wu, K.; Luo, Y.; Li, Y.; Zhang, C. Synthesis and acetone sensing properties of $ZnFe_2O_4$/rGO gas sensors. *Beilstein J. Nanotechnol.* **2019**, *10*, 2516–2526. [CrossRef]

30.   Salehi, T.; Taherizadeh, A.; Bahrami, A.; Allafchian, A.; Ghafarinia, V. Towards a Highly Functional Hybrid ZnO Nanofiber-rGO Gas Sensor. *Adv. Eng. Mater.* **2020**, *22*, 2000005. [CrossRef]

31.   Chang, Y.; Yao, Y.; Wang, B.; Luo, H.; Li, T.; Zhi, L. Reduced Graphene Oxide Mediated SnO_2 Nanocrystals for Enhanced Gas-sensing Properties. *J. Mater. Sci. Technol.* **2013**, *29*, 157–160. [CrossRef]

32.   Deng, S.; Tjoa, V.; Fan, H.; Tan, H.; Sayle, D.; Olivo, M.; Mhaisalkar, S.; Wei, J.; Sow, C. Reduced Graphene Oxide Conjugated Cu_2O Nanowire Mesocrystals for High-Performance NO_2 Gas Sensor. *J. Am. Chem. Soc.* **2012**, *134*, 4905–4917. [CrossRef] [PubMed]

33.   Johra, F.; Jung, W. RGO-TiO_2-ZnO composites: Synthesis, characterization, and application to photocatalysis. *Appl. Catal. A Gen.* **2015**, *491*, 52–57. [CrossRef]

34.   Yu, H.; Zhang, B.; Bulin, C.; Li, R.; Xing, R. High-efficient Synthesis of Graphene Oxide Based on Improved Hummers Method. *Sci. Rep.* **2016**, *6*, 36143. [CrossRef]

35.   Marcano, D.; Kosynkin, D.; Berlin, J.; Sinitskii, A.; Sun, Z.; Slesarev, A.; Alemany, L.; Lu, W.; Tour, J. Improved synthesis of graphene oxide. *ACS Nano* **2010**, *4*, 4806. [CrossRef]

36. Huynh, V.; Nguyen, M.; Nguyen, T.; Doan, B.; Le, T.; Dinh, N.; Nguyen, D.; Nguyen, A.; Le, M.; Hoang, M.; et al. Behavior of ZnO-doped TiO_2/rGO nanocomposite for water treatment enhancement. *Surf. Interfaces* **2021**, *23*, 100950.

37. Liao, D.; Badour, C.; Liao, B. Preparation of nanosized TiO_2/ZnO composite catalyst and its photocatalytic activity for degradation of methyl orange. *J. Mater. Chem. A* **2008**, *194*, 11–19. [CrossRef]

38. Divya, K.; Xavier, M.; Vandana, P.; Reethu, V.; Mathew, S. A quaternary TiO_2/ZnO/RGO/Ag nanocomposite with enhanced visible light photocatalytic performance. *New J. Chem.* **2017**, *10*, 1039.

39. Pan, X.; Yang, P.; Nan, H.; Yang, L.; Chen, H.; Zhao, X. Preparation and enhanced visible-light photoelectrocatalytic activity of ternary TiO_2-ZnO/RGO nanocomposites. *Electrochim. Acta* **2018**, *261*, 284–288. [CrossRef]

40. Rakkesh, R.; Balakumar, S. Facile synthesis of ZnO/TiO_2 core-shell nanostructures and their photocatalytic activities. *J. Nanosci. Nanotechnol.* **2013**, *13*, 370–376. [CrossRef]

41. Yang, D.; Velamakanni, A.; Bozoklu, G.; Park, S.; Stoller, M.; Piner, R.; Stankovich, S.; Jung, I.; Field, D.; Ventrice, C.; et al. Chemical analysis of graphene oxide films after heat and chemical treatments by X-ray photoelectron and Micro-Raman spectroscopy. *Carbon* **2009**, *47*, 145–152. [CrossRef]

42. Nurdiansah, H.; Susanti, D.; Firlyana, R.; Purwaningsih, H. Effect of rGO Addition Toward Photocatalyst Properties of ZnO/rGO/TiO_2 for Rhodamine B Degradation. *Mater. Sci. Forum* **2019**, *964*, 174–179. [CrossRef]

43. Huong, N.; Dat, N.; Thinh, D.; Anh, T.; MinhNguyet, D.; Quan, T.; Long, P.; Nam, H.; Phong, M.; Hieu, N. Optimization of the antibacterial activity of silver nanoparticles-decorated graphene oxide nanocomposites. *Synth. Met.* **2020**, *268*, 116492. [CrossRef]